Desalination and Water Treatment
www.deswater.com

doi: 10.5004/dwt.2023.29195

283 (2023) 196–208
January

Novel recyclable composite BiOBr/chitin-Fe_3O_4 with enhanced visible-light photocatalytic degradation of the antibacterial agent ciprofloxacin

Hongting Ye[a,b], Xiaoxing Zeng[a,b,*], Fei Feng[a], Yuanhang Li[a], Xiaofeng Gong[a,*]

[a]*School of Resources and Environment, Nanchang University, Nanchang 330047, China, Tel. 15907097445; email: xiaoxingzeng@ncu.edu.cn (X. Zeng), Tel. 18607910758; email: xfgong@ncu.edu.cn (X. Gong), Tel. 13037219155; email: 13037219155@163.com (H. Ye), Tel. 15180168688; email: fongfei@163.com (F. Feng), Tel. 18274838442; email: 759030222@qq.com (Y. Li)*
[b]*State Key Laboratory of Food Science and Technology, Nanchang University, Nanchang 330047, China*

Received 18 August 2022; Accepted 9 December 2022

ABSTRACT

In this study, novel recyclable composite BiOBr/chitin-Fe_3O_4 was synthesized by a solvothermal method using magnetic chitin chelating bismuth oxybromide (BiOBr) as precursor. The morphology, structure, photoelectric properties and chemical composition of the obtained samples were explored extensively by various characterization techniques. Due to the introduction of Fe_3O_4 and chitin, the composite BiOBr/chitin-Fe_3O_4 has multi-functions in enlarging photo response performance, reducing the band gap, increasing specific surface area and inhibiting recombination rate, which are essential to improve the photocatalytic efficiency. Using ciprofloxacin as target pollutant, the composite showed excellent photocatalytic performance under visible light irradiation, the apparent rate constant value of BiOBr/chitin-Fe_3O_4 is 5.8 times higher than that of pure BiOBr. The composite BiOBr/chitin-Fe_3O_4 could be recycled and reused conveniently and effectively, and the catalyst possessed good photocatalytic stability with the degradation efficiency remaining unchanged even after five times circle. The possible degradation mechanism was discussed on the basis of experiments.

Keywords: Bismuth oxybromide; BiOBr/chitin-Fe_3O_4; Ciprofloxacin (CIP); Pollutant; Photocatalytic

1. Introduction

Antibiotics have been widely used in both human therapy and veterinary application, which brought enormous benefits to human society [1–3]. However, amounts of antibiotic residues remained in the aquatic ecological system as a result of the abuse and ineffective disposal of antibiotics. These residues are hardly removed from waste water and easily accumulated, which have posed a great threaten to ecological systems and public health through food chains [4,5]. Therefore, employment of an effective method to remove the antibiotic residues is of great significance. Semiconductor photocatalysis technology as an advanced oxidation method has advantages of eco-friendliness, gentle reaction conditions, good selectivity and low energy-consuming [6,7], and thus has been recognized as a promising technique to eliminate organic contaminant in aquatic ecosystems. Catalyst is pivotal in the degradation of pollutants, so, the synthesis of highly efficient catalyst is the vital aspect of current photocatalysis research.

As a novel visible light photocatalyst, bismuth oxybromide (BiOBr) possesses a layered structure consisting of an alternating arrangement of $(Bi_2O_2)^{2+}$ slabs and double slabs of Br. It can provide enough large space to polarize orbitals and atoms, which are beneficial to improve migration efficiency of photoinduced carriers [8,9]. However, the pure BiOBr still has some limitations in practical application under visible light, such as poor photocatalytic performance due to

* Corresponding authors.

the rapid recombination of photoinduced carriers, the difficulty in recycling of smaller BiOBr nanoparticles in photocatalysis reaction system. To tackle the above-mentioned issues, many visible-light driven BiOBr-based composite photocatalysts have been studied and exhibited enhanced photocatalytic performance such as BiOBr/BiOI [10], Ag/AgBr/BiOBr [11], g-C_3N_4-BiOBr [12], BiOBr/$Bi_{24}O_{31}Br_{10}$ [13]. However, the difficulty of recovery and separation of the photocatalyst and producing secondary pollution also impede their particular application. Compositing with magnetic materials such as ferrite ($MnFe_2O_4$, $CoFe_2O_4$, $ZnFe_2O_4$, $NiFe_2O_4$, etc.), metal oxides (Mn_3O_4, Co_3O_4, Fe_3O_4, γ-Fe_2O_3, etc.) and pure metals (Fe, Co, etc.) can surmount this limitation [14–17]. Among these magnetic materials, Fe_3O_4 has been widely used to construct composite photocatalysts, due to its magnetism, especially its non-toxic, biocompatible and cost-effective properties [18,19]. However, the binding interaction between catalyst and magnetic component in the magnetic composites may be weak [20]. Therefore, it is worthwhile to investigate BiOBr-based composite that can make synergistic effect both for improving photocatalytic activity and convenient to reuse.

Chitin, a substance derived from crustacean shells, have been generally considered as a low-cost, resource-rich, nontoxic and renewable resource with the second most abundant biological resource after cellulose [21,22]. More importantly, the chitin containing plentiful of hydroxyl and amine functional groups, has special network structure and excellent adsorption [23,24]. It can be used as an effective modifier to adjust the terminal group and microstructure of composite and consequently alter the physical and chemical properties of materials. Meanwhile, chitin can chelate with metal ions or catalyst due to its multifunctional groups. Up to now, various materials related to chitin for the removal of pollutants in water have been reported in literatures [25,26]. Based on the above analysis, chitin as a renewable material not only can be used as chelating agent between Fe_3O_4 and BiOBr but also be used as an effective modifier and a high-capacity adsorbent in this composite.

To our knowledge, this is the first report concerning the construction of BiOBr/chitin-Fe_3O_4 composite. Compared with the pure BiOBr, the composite BiOBr/chitin-Fe_3O_4 exhibited enhanced photocatalytic activity for degradation ciprofloxacin, which is due to the physical and chemical properties of BiOBr can be modified by incorporating the chitin and synergistic effect of chitin and Fe_3O_4. Meanwhile, the introduction of Fe_3O_4 nanoparticles would make the composite easily separable and effectively recoverable by external magnetic field. Furthermore, the photocatalytic activity of the composite keeps stable even after five consecutive cycles. The low-cost, highly efficient composite BiOBr/chitin-Fe_3O_4 shows a broad application prospect in the treatment of wastewater without a secondary pollution.

2. Materials and methods

2.1. Materials and chemicals

Bismuth nitrate pentahydrate ($Bi(NO_3)_3{\cdot}5H_2O$, AR), ethylene glycol ($(HOCH_2)_2$, EG, AR), were obtained from Xilong Chemical Co., Ltd., (Shantou, China). Ciprofloxacin (CIP) was purchased from Aladdin (Shanghai, China). Chitin was purchased from Macklin Biochemical Co., Ltd., (Shanghai, China), and purified according to a previous report [27]. Fe_3O_4 nanoparticle was obtained from Aladdin (Shanghai, China). All reagents used in this work were of commercial analytical grade and could be used without further purification. Ultrapure water used throughout the whole work was produced by a Milli-Q Ultrapure Water System (Millipore, Bedford, USA).

2.2. Fabrication of BiOBr/chitin

BiOBr/chitin composites were prepared via hydrothermal method. 8 mmol $Bi(NO_3)_3{\cdot}5H_2O$ and 8 mmol KBr were slowly added dropwise to 60 mL of ethylene glycol, and then stirred until completely dissolved. Chitin solution was thereafter dropped into the mixed solution as a modifier. The resultant precursor solution was transferred to a 100 mL Teflon stainless-steel autoclave after further stirring for 1 h. The autoclave was placed in an oven set at 160°C for 16 h. The obtained precipitates obtained were washed several times with distilled water and absolute ethanol and dried at 60°C. Finally, the composite BiOBr/chitin was obtained.

2.3. Fabrication of BiOBr/chitin-Fe_3O_4

During the classical synthesis process, 8 mmol $Bi(NO_3)_3{\cdot}5H_2O$ and 8 mmol KBr were added to 60 mL of ethylene glycol under continuous stirring, then, chitin solution was dropped into the mixed solution. After further stirring for 1 h, nano-sized Fe_3O_4 was added in the above solution before ultrasonic dispersion for half an hour. The solution was then transferred to a 100 mL Teflon stainless-steel autoclave. The other steps were the same as above. Finally, BiOBr/chitin-Fe_3O_4 composites were obtained. The synthesis process of the BiOBr/chitin-Fe_3O_4 is illustrated inFig. 1.

2.4. Characterizations

X-ray diffraction (XRD) patterns were acquired by a Bede D1 System multifunction X-ray diffractometer employing Cu Kα (λ = 0.15418 nm) radiation. Scanning electron microscopy (SEM) images were taken on a Caisi Sigma 300 with Smart EDX emission scanning electron microscope. Transmission electron microscope (TEM) images were obtained via a FEI TF20 transmission electron microscope. X-ray photoelectron spectroscopy (XPS) measurements were conducted on Thermo Fisher Scientific Spectrometer using Al Ka radiation as the excitation source under vacuum at 2×10^6 Pa. Fourier-transform infrared (FT-IR) spectra were recorded at room temperature with a KBr pellet on Nicolet 5700 spectrometer. An Autosorb-2 analyzer was used to measure Brunauer–Emmett–Teller (BET) surface areas by N_2 adsorption–desorption isotherms. UV-Vis diffuse reflectance spectra were investigated on a TU-1900 spectrophotometer using $BaSO_4$ as a reference and were converted from reflection to absorbance by the Kubelka–Munk method. UV-Vis absorption spectra were determined by a Lingxi UV-3600 Plus Spectrophotometer. Fluorescence emission spectra were recorded on a Hitachi F-4500 type fluorescence

spectrophotometer with a 350 nm excitation source over a wavelength range of 400–600 nm. The magnetic property was examined by vibrating sample magnetometer (VSM) using Lake shore 7404 apparatus at 25°C with magnetic field of ±30,000 Oe.

2.5. Photodegradation experiments

The photocatalytic activity of the obtained products was investigated by degrading the colorless ciprofloxacin (CIP) solution using a 300 W Xe lamp with 420 nm cut off filter. Typically, 0.10 g prepared catalyst was dispersed into 250 mL aqueous solution of CIP (20 mg/L). Prior to irradiation, the suspension was treated by magnetically stirring in the dark for 40 min to reach adsorption–desorption equilibrium, the reaction time was 180 min after illumination. Meanwhile, take a water bath to keep constant room temperature. Subsequently, about 4 mL samples were taken once at intervals of every 20 min, after which the liquid was passed through a 0.22 μm filter membrane to remove the suspended solids. The CIP concentration was determined by UV-Vis spectrophotometer.

The photocatalytic degradation efficiency was calculated by the following formula:

$$\text{Removal} = \left(1 - \frac{C}{C_0}\right) \times 100\% \quad (1)$$

where C_0 and C are the initial and retained concentrations of CIP after adsorption equilibrium.

Photocatalytic degradation of CIP follows pseudo-first-order kinetics [28], which can be expressed as follows:

$$\ln\left(\frac{C_0}{C}\right) = kt \quad (2)$$

where k is the apparent reaction rate constant (min^{-1}).

2.6. Determination of active ingredients

To verify the active components in the catalytic reaction process, the isopropanol (IPA) and TEOA were added to investigate the hydroxyl radical ($^{\bullet}OH$) and hole (h^+) respectively. Nitro blue tetrazolium (NBT), with a concentration of 2.5×10^{-5} mol/L and a maximum absorption wavelength of 259 nm, was chosen to detect the presence of superoxide radical ($^{\bullet}O_2^-$). The procedure was similar to photocatalytic degradation with NBT replacing the pollutant CIP.

3. Result and discussion

3.1. XRD analysis

The XRD patterns of the obtained samples are shown in Fig. 2. As can be seen that all the diffraction peaks of the three samples were indexed as the tetragonal phase of BiOBr, the distinct peaks at 2θ = 10.90°, 25.15°, 31.69°, 32.22°, 39.38°, 46.2°, 50.67° and 57.11° are indexed to the (001), (101), (102), (110), (112), (200), (104) and (212) of the standard phase

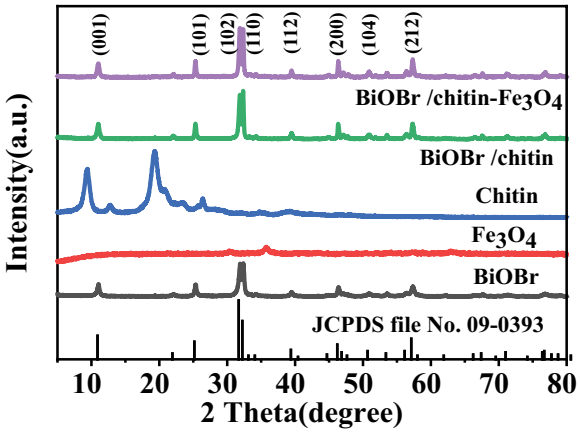

Fig. 2. XRD patterns of the obtained samples BiOBr, BiOBr/chitin, BiOBr/chitin-Fe_3O_4.

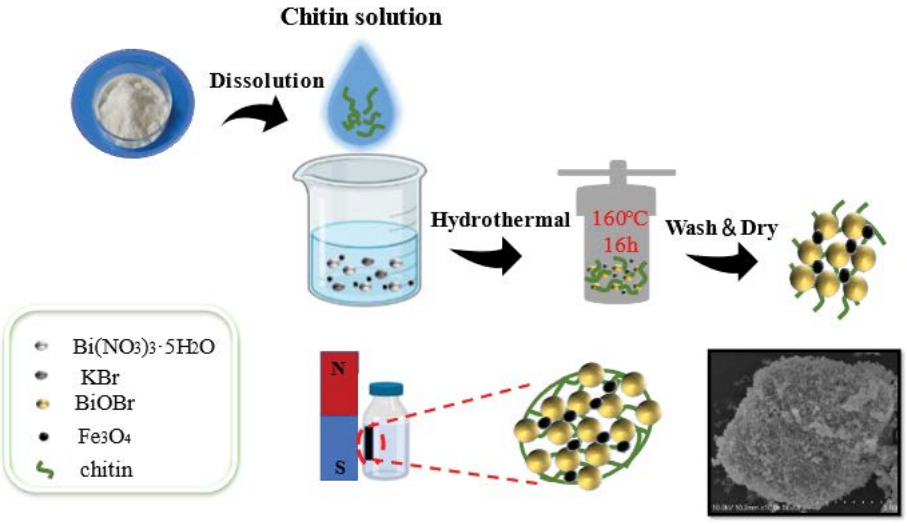

Fig. 1. Schematic illustration of formation process of BiOBr/chitin-Fe_3O_4.

(JCPDS file No.09-0393), respectively. However, the diffraction peak of chitin and Fe_3O_4 in BiOBr/chitin-Fe_3O_4 were not detected obviously, which was probably due to their low content. Compared with the pure BiOBr, the position of the diffraction peak of BiOBr/chitin-Fe_3O_4 composite did not shift, so the addition of chitin and Fe_3O_4 did not change the lattice composition of BiOBr after a series of functionalization processes. Further scrutinized, the diffraction peak intensity of BiOBr/chitin-Fe_3O_4 was higher than that of BiOBr obviously, illustrating BiOBr/chitin-Fe_3O_4 has better crystallinity. Moreover, the peak value of BiOBr (110) crystal surface was the highest in BiOBr/chitin. It can be speculated that chitin can effectively promote the formation of BiOBr (110) crystal surface and improve the photoactivity of composite BiOBr photocatalyst [29].

3.2. Morphology and microstructure analysis

The morphologies of the prepared samples are shown in Fig. 3a–f. The pure BiOBr was composed of stacked microspheres with a diameter of 2–4 nm assembled by nanosheets with a thickness of about 50 nm, it is worth noting that the sheet and sheet are tight. The morphologies of BiOBr/chitin and BiOBr/chitin-Fe_3O_4 were both composed of piles of incompact small particles and the interspace between the particles was relatively larger in comparison to the pure BiOBr. From Fig. 3c and d, a hierarchy structure could be further observed due to the particular network structure of chitin and BiOBr nanosheets formed three-dimensional porous structures of different levels. However, from Fig. 3e and f, the size of BiOBr/chitin-Fe_3O_4 and the interspace between the particles were relatively smaller than that of BiOBr/chitin, it may be nanoparticles Fe_3O_4 adhere to the surface of nanosheet and immobilized the hierarchical structure of composite.

The TEM and HRTEM images of the sample BiOBr/chitin-Fe_3O_4 are shown in Fig. 3g–i. The magnified crystal structure was displayed in Fig. 3g showing that the sample was consisted of thin BiOBr nanosheets and Fe_3O_4 nanoparticles. Fig. 3h and i showed the crystal (102) facet of BiOBr with *d* value 0.282 nm and crystal (110) facet of BiOBr with *d* value 0.277 nm. The energy spectrum (EDS) test of the sample confirmed the rough distribution of elements on the sample surface, as shown in Fig. 3j. The existence of C, N, O, Bi, Br and Fe could be observed in the samples from the EDS results, which demonstrated the successful introduction of chitin and Fe_3O_4 in BiOBr/chitin-Fe_3O_4.

3.3. XPS spectra

The surficial chemical information and electronic state of the obtained samples were characterized through XPS. As observed in Fig. 4a, the full spectrum confirms that the C, O, Bi, Br, N and Fe elements coexisted in the sample BiOBr/chitin-Fe_3O_4, in which the notably weak signal of Fe presumably was related to its extremely low amount. From the XPS spectra of the above elements in Fig. 4b–g, two distinct peaks centered on 159.3 and 164.6 eV were attributed to $Bi^{3+}4f_{7/2}$ and $4f_{5/2}$, respectively [30,31], the Br3d spectrum corresponded to 68.6 eV [32]. Compared with the XPS spectrum of BiOBr, the one peak in Br3d had a slight shift to lower binding energy in BiOBr/chitin, which could be ascribed to the interaction between Bi^{3+} and chitin nanofibers. The O1s peaks were resolved into two peaks at 529.6 and 531.2 eV, corresponding to the O^{2-} ions of BiOBr and Fe_3O_4 and adsorbed hydroxyl groups on the material surface, respectively [33]. The binding energies at 709.7 and 723.9 eV on the Fe2p spectrum were attributed to Fe^{2+} and Fe^{3+} ions respectively [34]. Fig. 4d illustrated the C1s peak could be resolved into three peaks at 284.4, 286.5 and 288.4 eV, which were ascribed to the C=C bonds, C–C bonds, and C–O bonds, respectively [35,36]. The peak of N1s at binding energy of 399.5 eV was also detected, which existed in chitin. Obviously, according to the above analysis, all elements of BiOBr/chitin-Fe_3O_4 composite were identified, confirming the successful formation of hybrid photocatalyst.

3.4. FT-IR and VSM analysis

The FT-IR spectra results of the obtained samples are depicted in Fig. 5a. For the pure BiOBr, the characteristic peak corresponded to 510 cm^{-1} was identified as the Bi–O stretching mode [37]. The spectrum of BiOBr/chitin-Fe_3O_4 depicted the other functional groups of containing C–O peak at 1,010 cm^{-1}, C–O–H peak at 1,376 cm^{-1}, N–H peak at 1562 cm^{-1} which were clearly visible [15]. The sharp peak at 2,835–3,008 cm^{-1} was allocated to $=CH_2$ and C–H bonds [32]. The broad bands at 3,430 and 1,620 cm^{-1} were ascribed to the O–H stretching and O–H bending vibration peak of adsorbed water molecules on the surface of the catalyst [38]. Meanwhile, Fe–O (580 cm^{-1}) peak was so weak that could hardly be observed. The characteristic peaks of BiOBr also appeared in the BiOBr/chitin and BiOBr/chitin-Fe_3O_4 with decreasing intensity and the incorporation of Fe_3O_4 and chitin made this peak slightly shift. This phenomenon that the appearance of characteristic peaks of carbon materials indicated BiOBr interacted with the –OH, C–O, or amide groups of the chitin nanofibers, which was consistent with XPS results, further indicating that there was extra carbon compound.

From Fig. 5b the magnetic property of BiOBr/chitin-Fe_3O_4 is characterized via vibrating sample magnetometer (VSM), suggesting that the saturation magnetization (M_s) of the composite was 10.56 emu/g and it had good superparamagnetic behavior and a typical s-type hysteresis loop due to the presence of Fe_3O_4 magnetite particles. Inset in Fig. 5b shows the photographs of BiOBr/chitin-Fe_3O_4 uniformly dispersed in water (left) and after applied a magnet outside the vessel (right). In consequence, the BiOBr/chitin-Fe_3O_4 can easily and effectively separate from solution within 60 s and recycle under external magnetic field [39].

3.5. BET analysis

As shown in Fig. 6, the pore structure of samples was characterized by using N_2 adsorption/desorption isotherms. In accordance with the IUPAC classification [40], all the three samples displayed typical type IV adsorption–desorption isotherms, referring the presence of mesoporous. In addition, the hysteresis loops of BiOBr/chitin and BiOBr/chitin-Fe_3O_4 were H3 type, indicating the presence of a slit shape with

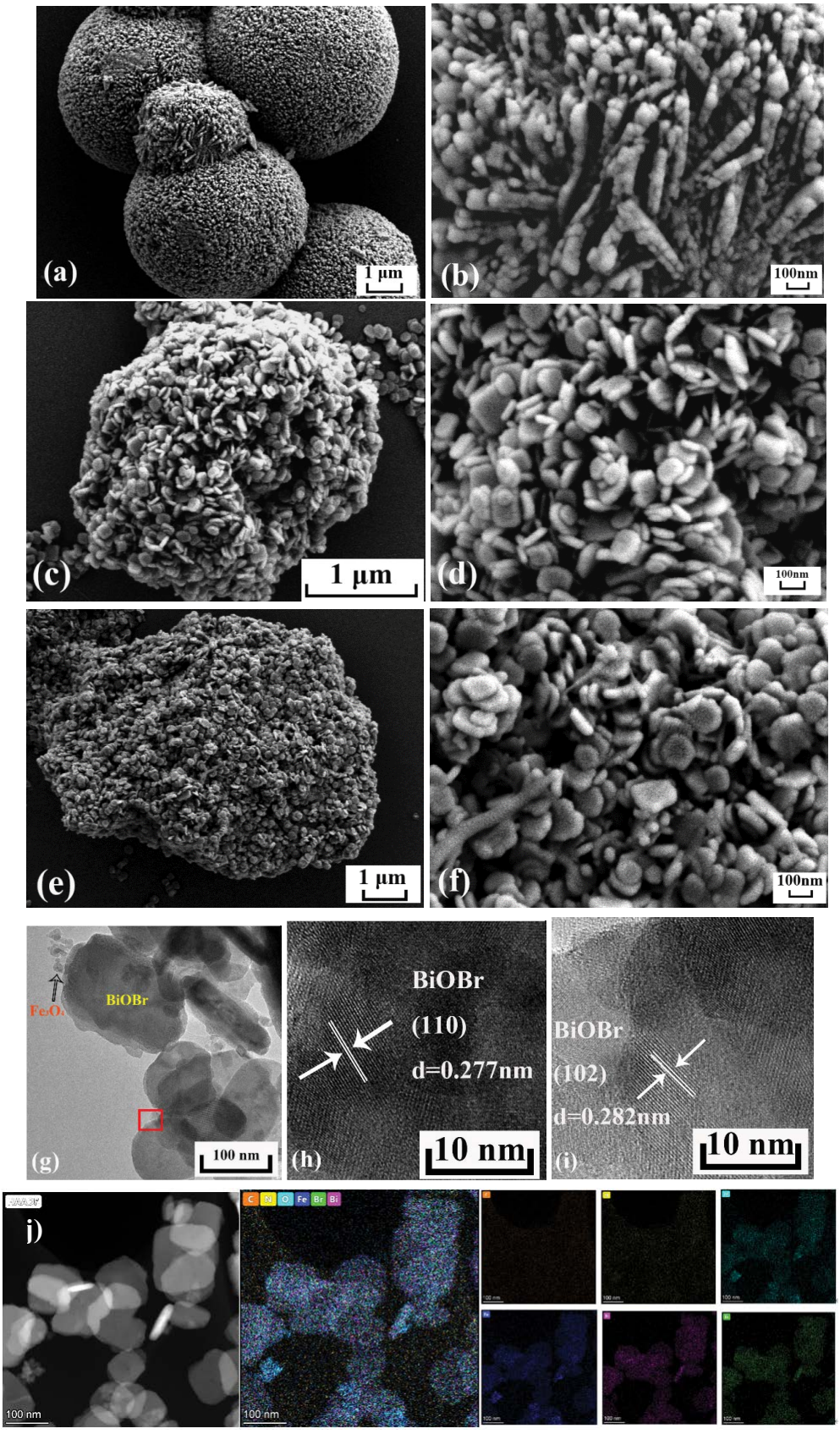

Fig. 3. SEM images of the obtained samples (a, b) BiOBr, (c, d) BiOBr/chitin, (e, f) BiOBr/chitin-Fe_3O_4, TEM of BiOBr/chitin-Fe_3O_4 (g–i) and elemental mappings and (j) BiOBr/chitin-Fe_3O_4.

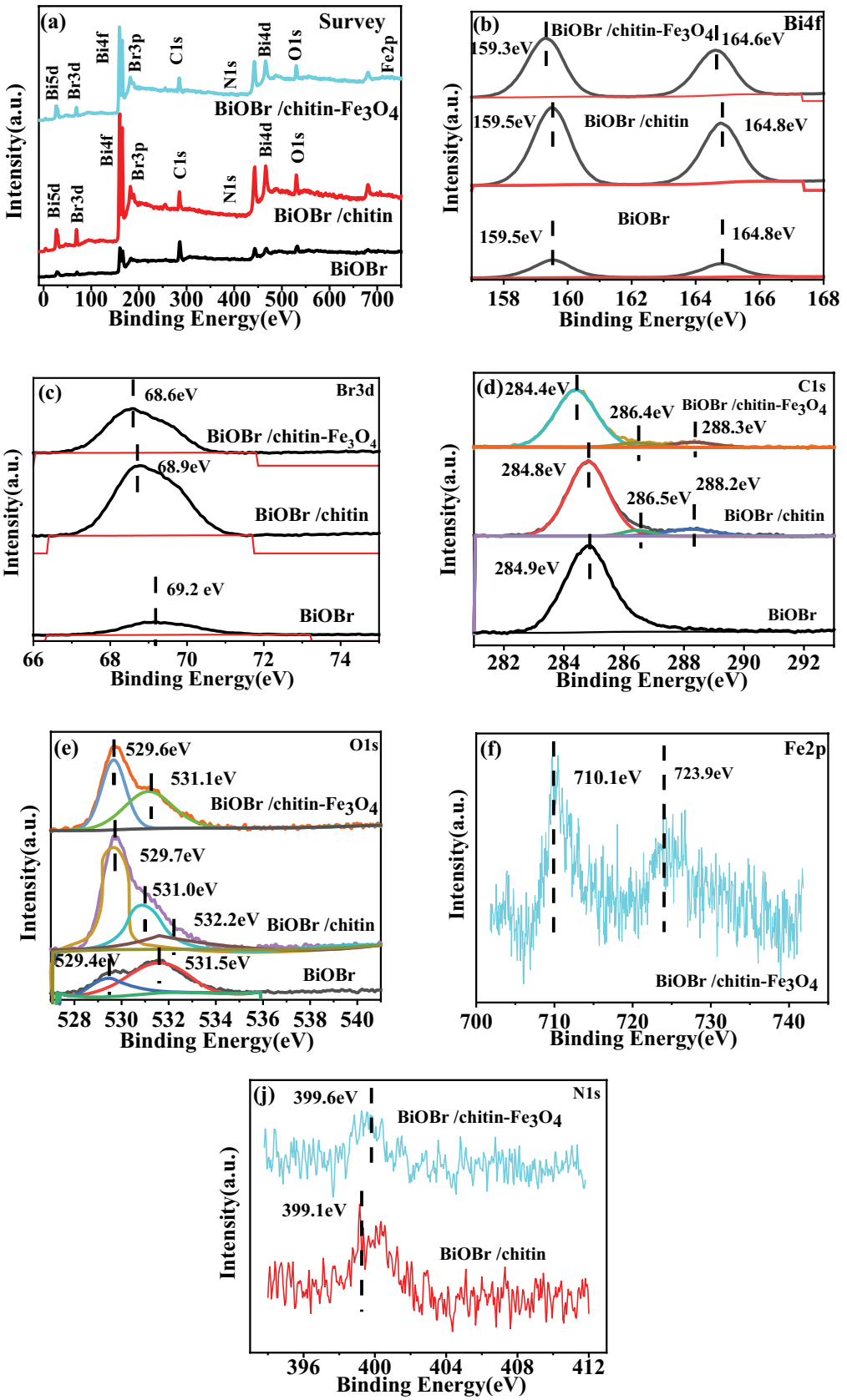

Fig. 4. Survey (a), Bi4f (b), Br3d (c), C1s (d), O1s (e), Fe2p (f), N1s (i), XPS spectra of the obtained samples BiOBr, BiOBr/chitin, BiOBr/chitin-Fe_3O_4.

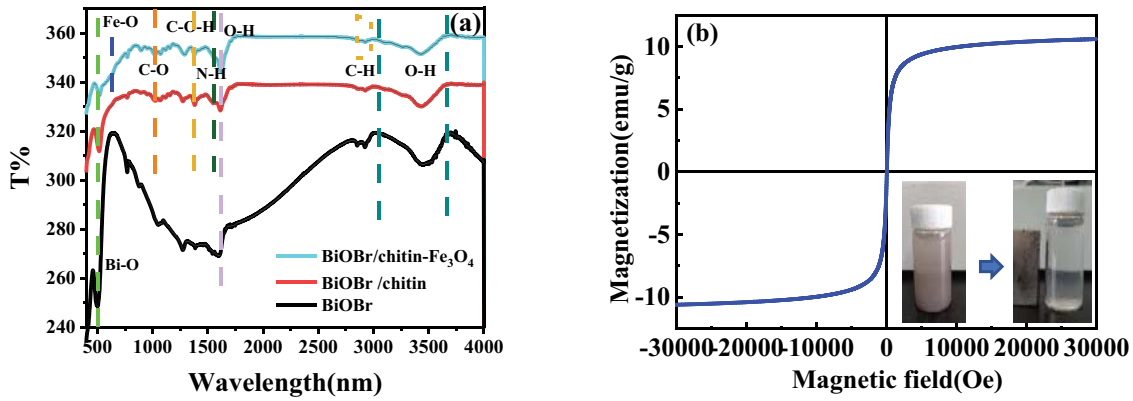

Fig. 5. FT-IR spectra of the obtained samples BiOBr, BiOBr/chitin, BiOBr/chitin-Fe_3O_4, (b) magnetization curves of the obtained samples BiOBr/chitin-Fe_3O_4. Inset: a photograph showing magnetic recycling of the BiOBr/chitin-Fe_3O_4 magnetic photocatalyst.

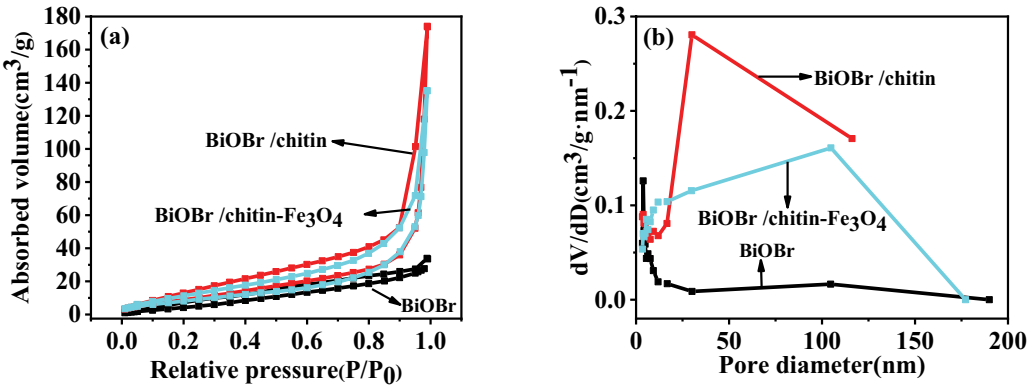

Fig. 6. N_2 adsorption–desorption isotherms (a) and pore-size distribution (b) of BiOBr, BiOBr/chitin, BiOBr/chitin-Fe_3O_4.

uneven size [41]. Apparently, the isotherms of BiOBr/chitin and BiOBr/chitin-Fe_3O_4 were very similar, proving that BiOBr/chitin and BiOBr/chitin-Fe_3O_4 had similar porous structures (Fig. 6a). The specific surface area for pure BiOBr, BiOBr/chitin and BiOBr/chitin-Fe_3O_4 were 23.13, 38.84 and 33.55 m^2/g, respectively. Introduction of the special network structure of chitin can modify the BiOBr, increasing the specific surface areas for BiOBr/chitin, but the specific surface area for BiOBr/chitin-Fe_3O_4 decreased which were probably owing to the Fe_3O_4 adhere on the chitin nanofibrous surface and immobilization of BiOBr.

Fig. 6b shows for BiOBr/chitin-Fe_3O_4 a hierarchical structure dominated by medium/large pores, and the pore size distribution was extended and continuous, the average pore sizes were 8.97, 27.74 and 24.92 nm, respectively, which is agreed with the previous specific surface area analysis. As well known, larger pore size and surface area can provide more active sites for photochemical reactions thus enhancing the photocatalytic performance [42].

3.6. UV-Vis diffuse reflectance spectroscopy analysis

The optical properties of the obtained samples were studied by ultraviolet-to-visible diffuse reflectance spectroscopy (UV-Vis DRS). The UV-Vis diffuse reflectance spectra of samples are depicted in Fig. 7a, indicating that all the three samples have superior absorption visible light ability with wavelengths above 420 nm and no impurity peak appears. It has been reported that the visible light intensity of xenon lamp in the wavelength range of 500–600 nm is greater than below 500 nm [43]. Therefore, the absorption of xenon lamp light source of sample BiOBr/chitin-Fe_3O_4 was more sufficient than that of samples BiOBr/chitin and BiOBr. The absorption band boundary values of pure BiOBr, BiOBr/chitin and BiOBr/chitin-Fe_3O_4 were close to 472, 483 and 492nm, respectively (Fig. 7a). The increase of the absorption band edge value for BiOBr/chitin-Fe_3O_4 was ascribed to the uniform distribution of BiOBr on the chitin nanofibers and the improvement of the absorption sites, in the case of Fe_3O_4 nanoparticles also enhance the absorption band of BiOBr. The energy band gap of the catalyst can be calculated by the following formula [44]:

$$\alpha\left(E_{\text{photon}}\right) = A\left(E_{\text{photon}} - E_{\text{photon}}\right)^{n/2} \tag{3}$$

where E_g, α, E_{photon}, A are the band gap width (eV), the absorption coefficient (cm^{-1}), the photon energy (eV), and a constant, respectively. N is equal to 4 for indirect band gap and 1 for direct band gap. The obtained catalyst is indirect band gap catalyst. The band gap of the catalyst is obtained from the E_{photon} curve corresponding to $(\alpha \cdot E_{\text{photon}})^{1/2}$ in Fig. 7b.

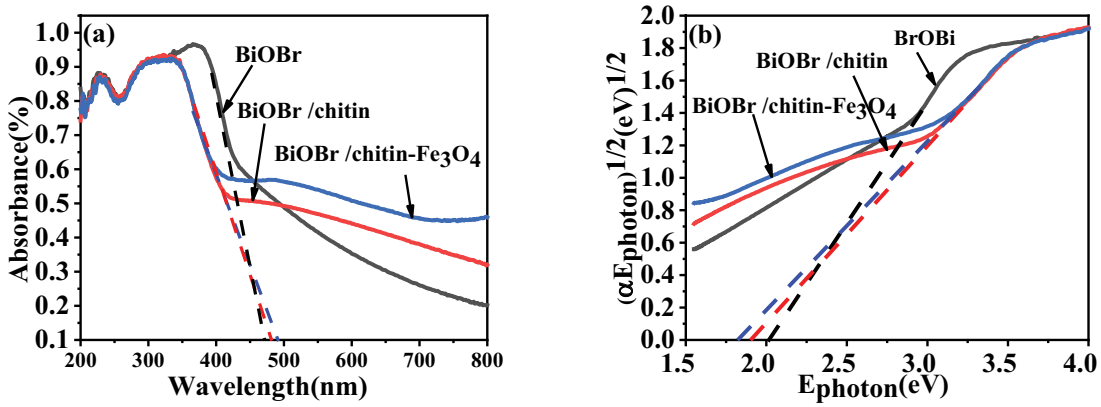

Fig. 7. (a) UV-Vis DRS absorption spectra, (b) $(\alpha \cdot E_{photon})^{1/2} - E_{photon}$ curves of the BiOBr, BiOBr/chitin, BiOBr/chitin-Fe_3O_4.

By extrapolation, the E_g value of BiOBr/chitin is 1.82 eV, the E_g value of BiOBr/chitin-Fe_3O_4 is 1.68 eV (Table 1), which both has a narrower band gap than BiOBr (2.78–2.93 eV) reported in literature. The results further prove that chitin and Fe_3O_4 can synergistically increase sensitivity to visible light and narrow the band gap of BiOBr, which are greatly conducive to improve the photocatalytic activity.

3.7. Photoluminescence analysis

Photoluminescence (PL) emission analysis was carried out to examine the separation capability of photogenerated electron–hole pairs. Weaker PL emission intensity indicates lower recombination rate of e^- and h^+ and higher photocatalytic activity of the photogenerated carrier [45,46]. The PL spectra of BiOBr, BiOBr/chitin and BiOBr/chitin-Fe_3O_4 is shown in Fig. 8. It is observed that BiOBr/chitin-Fe_3O_4 has the weakest luminescence intensity, elucidating that the modification of chitin and Fe_3O_4 significantly reduced the possibility of photoinduced hole-electron recombination, promoted the charge transfer, thus improving the photocatalytic performance.

3.8. Photocatalyst activity analysis

The photocatalytic degradation abilities of the obtained samples for an aqueous solution of CIP were investigated in the visible region. Fig. 9a shows the changes of absorption spectra of CIP solution with reaction time in the presence of BiOBr/chitin-Fe_3O_4 composite. In the presence of other two catalysts, the peak shape of absorption spectra of ciprofloxacin solution is the same as Fig. 9a. Clearly, the intensity of absorption peak was becoming weaker and weaker with increasing reaction time. Finally, the absorption peak of CIP at 276 nm nearly disappeared after irradiation for 180 min, signifying that BiOBr/chitin-Fe_3O_4 possesses excellent photocatalytic activity.

Fig. 9b shows the removal efficiency of BiOBr/chitin and BiOBr/chitin-Fe_3O_4 after 180 min can reach 77.77% and 79.46% and only 21.76% of the CIP was decomposed after irradiation for 180 min when pure BiOBr was used as a photocatalyst. The kinetic liner relationship of degradation of CIP as a function of the obtained samples were shown in

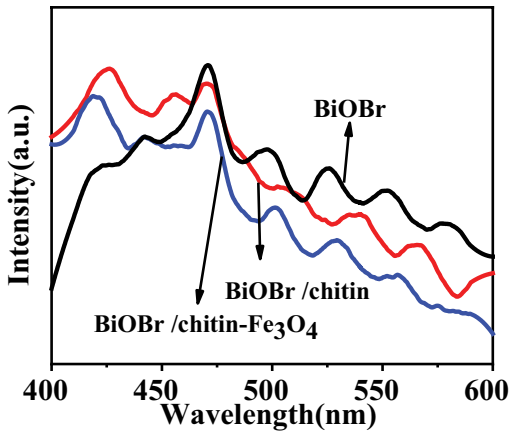

Fig. 8. PL spectra of the obtained samples BiOBr, BiOBr/chitin, BiOBr/chitin-Fe_3O_4.

Fig. 9c and the values were shown in Table 1. The photodegradation first-order reaction rate constants of BiOBr/chitin and BiOBr/chitin-Fe_3O_4 for CIP are 5.2 and 5.8 times higher than that of the pure BiOBr, respectively. Higher photodegradation rate constant signifies better photocatalytic activity [47]. Based on the above characterization of the samples, the excellent photocatalytic degradation efficiencies of the sample BiOBr/chitin-Fe_3O_4 can be ascribed to the followings: firstly, the porous architecture and the large specific surface area enable adequate pollutants-catalyst contact and adsorb more active species, which are conducive to promote photocatalytic performance. Secondly, synergistic effect of Fe_3O_4 and chitin favored more efficient charge transferring and prolonged the lifetime of the photogenerated holes-electrons. Thirdly, BiOBr/chitin-Fe_3O_4 showed stronger adsorption peak, lower bandgap energy and longer wavelength.

The effect of different dosages of BiOBr/chitin-Fe_3O_4 on the degradation efficiency of CIP is shown in Fig. 9d. The efficiency for CIP removal increased rapidly from 49.69% to 79.46% as the catalyst dosage added from 50 to 100 mg. Obviously, as the dosage increased, more active sites were exposed, more h^+ and e^- were produced which could generate more active species and better visible light response was performed. However, while the dosage of BiOBr/

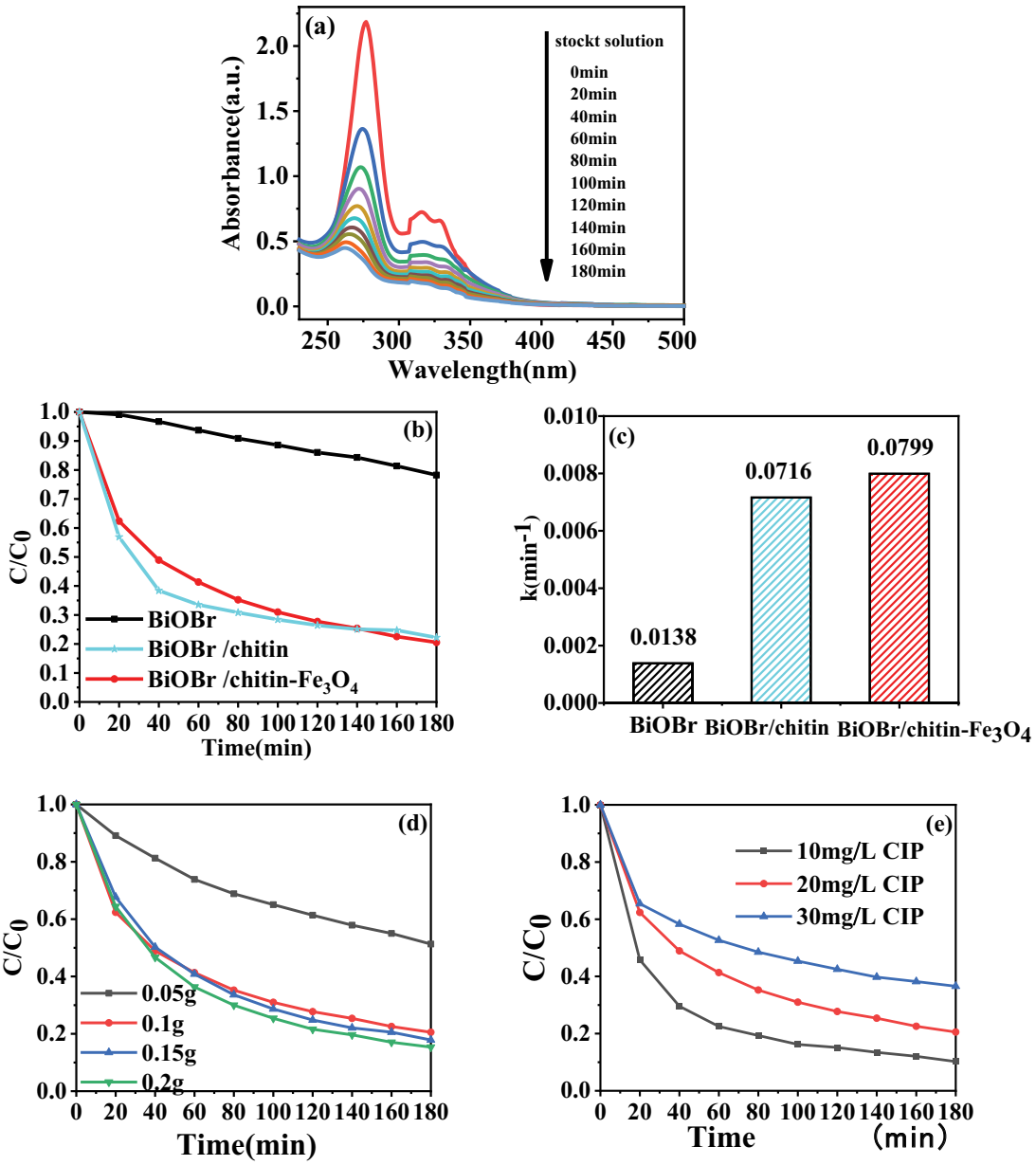

Fig. 9. Temporal UV-Vis absorption spectral changes of CIP solution as a function of irradiation time in the presence of the samples (a), photocatalytic performance of BiOBr/chitin, BiOBr/chitin-Fe_3O_4 samples (b) for CIP solution degradation and different degradation rate for CIP solution degradation containing 100 mg of BiOBr, BiOBr/chitin, BiOBr/chitin-Fe_3O_4 samples (c), photocatalytic efficiency of different dosages of BiOBr/chitin-Fe_3O_4 towards CIP (20 mg/L) and (d) after 180 min and photocatalytic efficiency of BiOBr/chitin-Fe_3O_4 (100 mg) towards different concentrations of CIP (e) after 180 min.

chitin-Fe_3O_4 reached to a certain amount, the active sites were saturated by contacting with contaminants, the catalytic activity was no longer significantly improved. There was just a slight improvement of degradation efficiency as the dosage increased from 100 mg to 200 mg. Considering the cost consumption and catalytic performance, the optimal photocatalytic dosage was 100 mg.

Using BiOBr/chitin-Fe_3O_4 (100 mg) as photocatalyst, the effect of different initial concentrations of CIP were investigated and the results are shown in Fig. 9e. As the initial concentration increased, the photodegradation efficiency decreased, due to the catalytic sites were covered with CIP of high initial concentrations and more pollutants competed for catalytic sites. Moreover, it is difficult for visible light to reach the catalytic surface for reaction at a high initial concentration.

3.9. Photocatalytic degradation mechanisms

To systematically understand the photocatalytic degradation mechanisms, various crucial active species generated in the process of CIP photodegradation over BiOBr/chitin-Fe_3O_4 were studied by radical trapping experiments. Generally, IPA is used as a quencher of hydroxyl radicals

(•OH) and TEOA is used as a scavenger of photo-excited holes (h^+), respectively. The results are shown in Fig. 10a, after adding 1 mM IPA to the solution containing BiOBr/chitin-Fe_3O_4, the degradation efficiency was declined of approximately 20% in comparison to no quencher, indicating there was formation of •OH during the photocatalytic reaction. When 1 mM TEOA was added to the solution containing BiOBr/chitin-Fe_3O_4, the degradation efficiency was declined of 45% in comparison to no scavenger, this indicated that h^+ played an important role in photocatalysis. Finally, NBT replaced the targeted contaminant CIP was used to verify the presence of $^{\bullet}O_2^-$ in the photocatalytic system. As depicted in Fig. 10b, the downtrend of absorption spectra of NBT solution with increasing degradation time under visible light irradiation illustrated that $^{\bullet}O_2^-$ was generated in the photocatalytic reaction.

Fig. 10c explains the CIP degradation process caused by BiOBr/chitin-Fe_3O_4 composites. The sample BiOBr/chitin-Fe_3O_4 could generate holes and electrons under visible light irradiation [Eq. (I)]. Then the electrons can react with the adsorbed O_2 to produce $^{\bullet}O_2^-$ [Eq. (II)]. Meanwhile, the hydroxyl group in the water molecule is also created [Eq. (III)].

$$\text{BiOBr / chitin - } Fe_3O_4 + h\nu \rightarrow h^+ + e \quad \text{(I)}$$

$$O_2 + e \rightarrow \bullet O_2^- \quad \text{(II)}$$

$$H_2O + e \rightarrow \bullet OH + H^+ \quad \text{(III)}$$

The CIP can be oxidized to the final products such as CO_2 with the action of photogenerated holes (h^+), hydroxide radical (•OH) and superoxide radical ($^{\bullet}O_2^-$) [Eq. (IV)].

$$\text{CIP} + h^+ + {}^{\bullet}O_2^- + {}^{\bullet}OH \rightarrow CO_2 + H_2O + \text{Small molecular} \quad \text{(IV)}$$

3.10. Photocatalyst stability

The photocatalytic stability of catalyst is vital to evaluate its practical application, and thus, five rounds of recycling experiments were conducted using the obtained product BiOBr/chitin-Fe_3O_4. After the completion of each experiment, this work used a magnet to collect BiOBr/chitin-Fe_3O_4, then washed and dried at 70°C for 6 h, finally applied in the next run. The degradation efficiency is almost stable even after the fifth recycle as shown in Fig. 11a, just a slightly decrease due to the little loss of photocatalyst in the recycle degradation process. Moreover, the XRD results of BiOBr/chitin-Fe_3O_4 before and after reaction are plotted

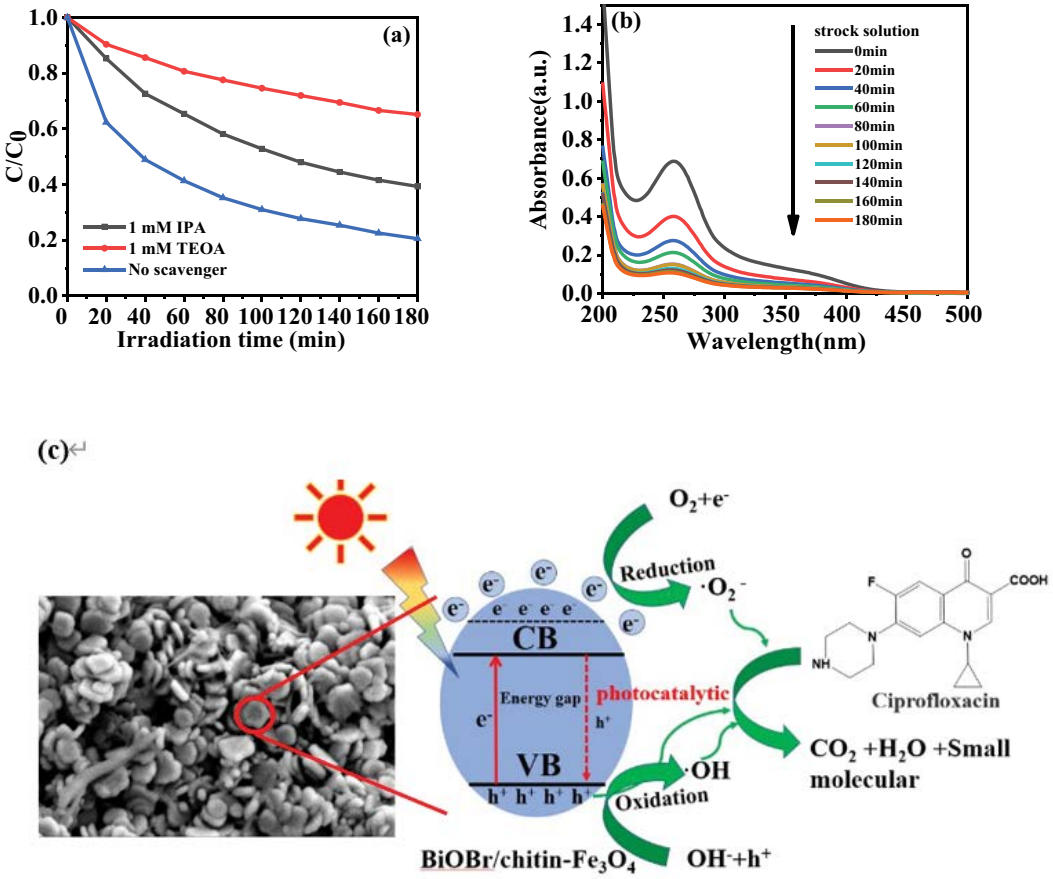

Fig. 10. (a) Photodegradation performance for CIP solution by BiOBr/chitin-Fe_3O_4 in the presence of various radical scavengers and (b) UV-Vis absorption spectra of NBT in the BiOBr/chitin-Fe_3O_4 suspension and (c) the scheme of illustrating the photocatalytic mechanism.

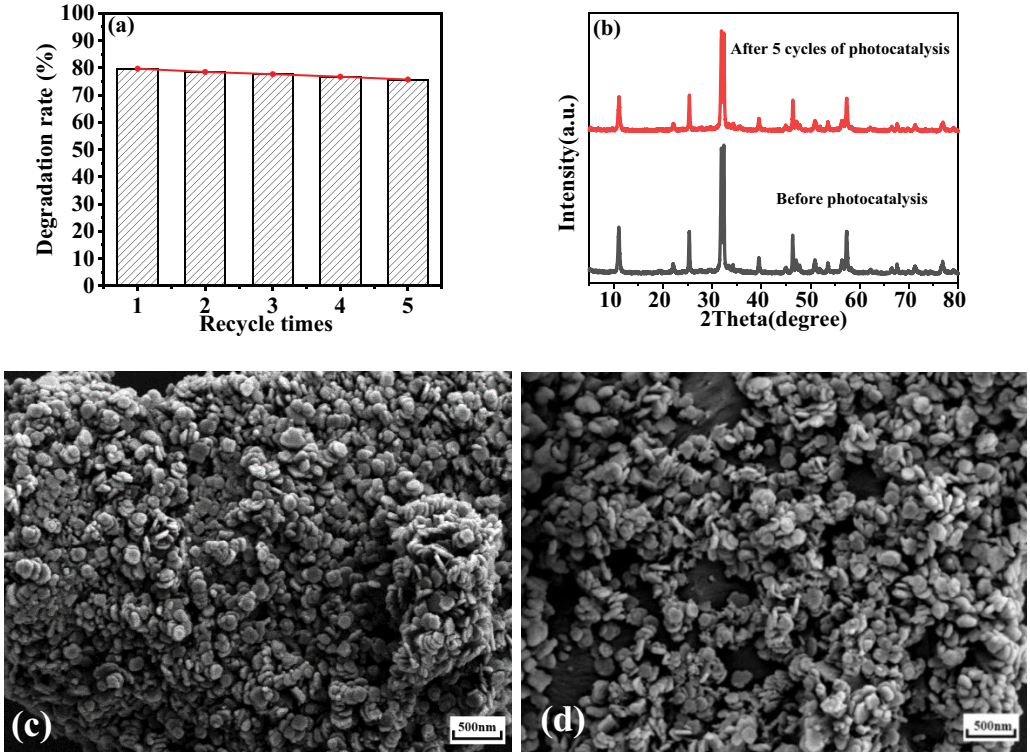

Fig. 11. Reusability of BiOBr/chitin-Fe_3O_4 (100 mg) for the photodegradation of CIP (C = 20 mg/L, 250 mL) (a) and SEM spectra before and after 5 cycles of BiOBr/chitin-Fe_3O_4 photocatalysis (b).

Table 1
E_g and k values of the obtained samples

Sample	E_g (eV)	k (min^{-1})
BiOBr	2.03	0.00138
BiOBr/chitin	1.82	0.00716
BiOBr/chitin-Fe_3O_4	1.68	0.00799

in Fig. 11b. The characteristic peaks of BiOBr/chitin-Fe_3O_4 were unchanged. Meanwhile, the morphology of BiOBr/chitin-Fe_3O_4 was explored after five cycles. It can be seen from Fig. 11c and d, the morphology before and after five cycles were nearly identical, which further indicating that BiOBr/chitin-Fe_3O_4 has good structural stability. Therefore, the composite BiOBr/chitin-Fe_3O_4 shows long-term stability and exhibits convenient recyclability for the photocatalytic degradation of organic pollutants.

4. Conclusion

In summary, a novel environmental-friendly composite BiOBr/chitin-Fe_3O_4 was successfully fabricated by a simple solvothermal method. The composite BiOBr/chitin-Fe_3O_4 exhibited the best photocatalytic performance for degradation of the antibacterial agent ciprofloxacin under visible light irradiation. The excellent photocatalytic activity of BiOBr/chitin-Fe_3O_4 benefits from the increased separation of photogenerated electrons and hole pairs, enlarged specific surface area and enhanced light capture due to the modification and synergistic effect of chitin and Fe_3O_4. It can be inferred that $^{\bullet}O_2^-$, $^{\bullet}OH$ and h^+ are the main active ingredients in the degradation process from radical trapping experiments. Furthermore, the BiOBr/chitin-Fe_3O_4 also shows great recyclability and stability during the photocatalysis of CIP.

Conflict of interest

The authors declare there is no conflict of interest.

Acknowledgement

The authors are grateful for the financial support from the Open Project Program of State Key Laboratory of Food Science and Technology, Nanchang University (No. SKLF-KF-202012.)

References

[1] M. Bilal, S.S. Ashraf, D. Barceló, H.M.N. Iqbal, Biocatalytic degradation/redefining "removal" fate of pharmaceutically active compounds and antibiotics in the aquatic environment, Sci. Total Environ., 691 (2019) 1190–1211.
[2] B. Petrie, R. Barden, B. Kasprzyk-Hordern, A review on emerging contaminants in wastewaters and the environment: current knowledge, understudied areas and recommendations for future monitoring, Water Res., 72 (2015) 3–27.
[3] H. Luo, Y. Zeng, Y. Cheng, D. He, X. Pan, Activation of peroxymonosulfate by iron oxychloride with hydroxylamine for

ciprofloxacin degradation and bacterial disinfection, Sci. Total Environ., 799 (2021) 149506, doi: 10.1016/j.scitotenv.2021.149506.
[4] J. Xu, X. Li, J. Niu, M. Chen, J. Yue, Synthesis of direct Z-Scheme Bi_3TaO_7/CdS composite photocatalysts with enhanced photocatalytic performance for ciprofloxacin degradation under visible light irradiation, J. Alloys Compd., 834 (2020) 155061, doi: 10.1016/j.jallcom.2020.155061.
[5] L. Yang, Y. Luo, L. Yang, S. Luo, X. Luo, W. Dai, T. Li, Y. Luo, Enhanced photocatalytic activity of hierarchical titanium dioxide microspheres with combining carbon nanotubes as "e-bridge", J. Hazard. Mater., 367 (2019) 550–558.
[6] B. Weng, M. Qi, C. Han, Z. Tang, Y. Xu, Photocorrosion inhibition of semiconductor-based photocatalysts: basic principle, current development, and future perspective, ACS Catal., 9 (2019) 4642–4687.
[7] R. Dai, L. Zhang, J. Ning, W. Wang, Q. Wu, J. Yang, F. Zhang, J.-a. Wang, New insights into tuning BiOBr photocatalysis efficiency under visible-light for degradation of broad-spectrum antibiotics: synergistic calcination and doping, J. Alloys Compd., 887 (2021) 161481, doi: 10.1016/j.jallcom.2021.161481.
[8] J. Shang, W. Hao, X. Lv, Bismuth oxybromide with reasonable photocatalytic reduction activity under visible light, ACS Catal., 4 (2014) 954–961.
[9] S. Qu, Y. Xiong, J. Zhang, Graphene oxide and carbon nanodots co-modified BiOBr nanocomposites with enhanced photocatalytic 4-chlorophenol degradation and mechanism insight, J. Colloid Interface Sci., 527 (2018) 78–86.
[10] H. Huang, X. Han, X. Li, S. Wang, P.K. Chu, Y. Zhang, Fabrication of multiple heterojunctions with tunable visible-light-active photocatalytic reactivity in BiOBr-BiOI full-range composites based on microstructure modulation and band structures, ACS Appl. Mater. Interfaces, 7 (2015) 482–492.
[11] H. Cheng, B. Huang, P. Wang, Z. Wang, Z. Lou, J. Wang, X. Qin, X. Zhang, Y. Dai, *In-situ* ion exchange synthesis of the novel Ag/AgBr/BiOBr hybrid with highly efficient decontamination of pollutants, Chem. Commun. (Cambridge, U.K.), 47 (2011) 7054–7056.
[12] Y. Hou, Y. Gan, Z. Yu, X. Chen, L. Qian, B. Zhang, L. Huang, J. Huang, Solar promoted azo dye degradation and energy production in the bio-photoelectrochemical system with a g-C_3N_4/BiOBr heterojunction photocathode, J. Power Sources, 371 (2017) 26–34.
[13] X. Zeng, Y. Wan, X. Gong, Z. Xu, Additive dependent synthesis of bismuth oxybromide composites for photocatalytic removal of the antibacterial agent ciprofloxacin and mechanism insight, RSC Adv., 7 (2017) 36269–36278.
[14] X. Jiang, D. Kong, B. Luo, M. Wang, D. Zhang, X. Pu, Preparation of magnetically retrievable flower-like AgBr/BiOBr/$NiFe_2O_4$ direct Z-scheme heterojunction photocatalyst with enhanced visible-light photoactivity, Colloids Surf., A, 33 (2022) 127880, doi: 10.1016/j.colsurfa.2021.127880.
[15] M. Zheng, X. Ma, J. Hu, X. Zhang, D. Li, W. Duan, Novel recyclable BiOBr/Fe_3O_4/RGO composites with remarkable visible-light photocatalytic activity, RSC Adv., 10 (2020) 19961–19973.
[16] L. Cao, D. Ma, Z. Zhou, C. Xu, C. Cao, P. Zhao, Q. Huang, Efficient photocatalytic degradation of herbicide glyphosate in water by magnetically separable and recyclable BiOBr/Fe_3O_4 nanocomposites under visible light irradiation, Chem. Eng. J. (Lausanne), 368 (2019) 212–222.
[17] X. Jiang, Z. Wang, M. Zhang, M. Wang, R. Wu, X. Shi, B. Luo, D. Zhang, X. Pu, H Li, A novel direct Z-scheme heterojunction $BiFeO_3$/$ZnFe_2O_4$ photocatalyst for enhanced photocatalyst degradation activity under visible light irradiation, J. Alloys Compd., 912 (2022) 165185, doi: 10.1016/j.jallcom.2022.165185.
[18] P. Xu, G.M. Zeng, D.L. Huang, C. Lai, Z. Wei, C. Huang, G.X. Xie, Z.F. Liu, C.L. Feng, Use of iron oxide nanomaterials in wastewater treatment: a review, Sci. Total Environ., 424 (2012) 1–10.
[19] S. Li, Z. Wang, X. Zhao, X. Yang, G. Liang, X. Xie, Insight into enhanced carbamazepine photodegradation over biochar-based magnetic photocatalyst Fe_3O_4/BiOBr/BC under visible LED light irradiation, Chem. Eng. J. (Lausanne), 360 (2019) 600–611.
[20] L. Zhang, J. Lian, L. Wu, Z. Duan, J. Jiang, L. Zhao, Synthesis of a thin-layer MnO_2 nanosheet-coated Fe_3O_4 nanocomposite as a magnetically separable photocatalyst, Langmuir, 30 (2014) 7006–7013.
[21] S. Choy, H.T. Bui, D.V. Lam, S.M. Lee, W. Kim, D.S. Hwang, Photocatalytic exoskeleton: chitin nanofiber for retrievable and sustainable TiO_2 carriers for the decomposition of various pollutants, Carbohydr. Polym., 271 (2021) 118413, doi: 10.1016/j.carbpol.2021.118413.
[22] V.V. Bazhenov, M. Wysokowski, I. Petrenko, D. Stawski, P. Sapozhnikov, R. Born, A.L. Stelling, S. Kaiser, T. Jesionowski, Preparation of monolithic silica-chitin composite under extreme biomimetic conditions, Int. J. Biol. Macromol., 76 (2015) 33–38.
[23] S. Wu, B.D., A. Lu, Y. Wang, Q. Ye, L. Zhang, Biocompatible chitin/carbon nanotubes composite hydrogels as neuronal growth substrates, Carbohydr. Polym., 174 (2017) 830–840.
[24] K. Vimal Kumar, B.V. Appa Rao, N.Y. Hebalkar, Phosphorylated chitin as a chemically modified polymer for ecofriendly corrosion inhibition of copper in aqueous chloride environment, Res. Chem. Intermed., 43 (2017) 5811–5828.
[25] M. Liu, Y. Zhang, J. Li, C. Zhou, Chitin-natural clay nanotubes hybrid hydrogel, Int. J. Biol. Macromol., 58 (2013) 23–30.
[26] X. Lin, A. Yang, G. Huang, X. Zhou, Y. Zhai, X. Chen, E. McBean, Treatment of aquaculture wastewater through Chitin/ZnO composite photocatalyst, Water, 11 (2019), doi: 10.3390/w11020310.
[27] B. Duan, X. Zheng, Z. Xia, X. Fan, L. Guo, J. Liu, Y. Wang, Q. Ye, L. Zhang, Highly biocompatible nanofibrous microspheres self-assembled from chitin in NaOH/urea aqueous solution as cell carriers, Angew. Chem. Int. Ed., 54 (2015) 5152–5156.
[28] J. Xu, W. Meng, Y. Zhang, L. Li, C. Guo, Photocatalytic degradation of tetrabromobisphenol A by mesoporous BiOBr: efficacy, products and pathway, Appl. Catal., B, 107 (2011) 355–362.
[29] Y. Peng, J. Xu, T. Liu, Y.G. Mao, Controlled synthesis of one-dimensional BiOBr with exposed (110) facets and enhanced photocatalytic activity, CrystEngComm, 19 (2017) 6473–6480.
[30] P. Li, Z. Zhou, Q. Wang, M. Guo, S. Chen, J. Low, R. Long, W. Liu, P. Ding, Y. Wu, Y. Xiong, Visible-light-driven nitrogen fixation catalyzed by Bi_5O_7Br nanostructures: enhanced performance by oxygen vacancies, J. Am. Chem. Soc., 142 (2020) 12430–12439.
[31] Y. Liu, J. Li, J. Li, X. Yan, F. Wang, W. Yang, D.H.L. Ng, J. Yang, Active magnetic Fe^{3+}-doped BiOBr micromotors as efficient solar photo-fenton catalyst, J. Cleaner Prod., 252 (2020) 119573, doi: 10.1016/j.jclepro.2019.119573.
[32] X. Xie, S. Li, K. Qi, Z. Wang, Photoinduced synthesis of green photocatalyst Fe_3O_4/BiOBr/CQDs derived from corncob biomass for carbamazepine degradation: the role of selectively more CQDs decoration and Z-scheme structure, Chem. Eng. J. (Lausanne), 420 (2021) 129705, doi: 10.1016/j.cej.2021.129705.
[33] Y. Wu, H. Ji, Q. Liu, Z. Sun, P. Li, P. Ding, M. Guo, X. Yi, W. Xu, C. Wang, S. Gao, Q. Wang, W. Liu, S. Chen, Visible light photocatalytic degradation of sulfanilamide enhanced by Mo doping of BiOBr nanoflowers, J. Hazard. Mater., 424 (2021) 127563, doi: 10.1016/j.jhazmat.2021.127563.
[34] X. Yang, X. Zhang, Z. Wang, S. Li, J. Zhao, G. Liang, X. Xie, Mechanistic insights into removal of norfloxacin from water using different natural iron ore – biochar composites: more rich free radicals derived from natural pyrite-biochar composites than hematite-biochar composites, Appl. Catal., B, 255 (2019) 117752, doi: 10.1016/j.apcatb.2019.117752.
[35] Y. Zhou, T. Cai, S. Liu, Y. Liu, H. Chen, Z. Li, J. Du, Z. Lei, H. Peng, N-doped magnetic three-dimensional carbon microspheres@TiO_2 with a porous architecture for enhanced degradation of tetracycline and methyl orange via adsorption/photocatalysis synergy, Chem. Eng. J. (Lausanne), 411 (2021) 128615, doi: 10.1016/j.cej.2021.128615.
[36] F. Wang, L. Liang, L. Shi, M. Liu, J. Sun, CO_2-assisted synthesis of mesoporous carbon/C-doped ZnO composites for enhanced photocatalytic performance under visible light, Dalton Trans., 43 (2014) 16441–16449.
[37] Y. Jin, Z. Lu, P. Zhang, F. Li, T. Li, L. Zhang, W. Fan, C. Hu, Enhanced photocatalytic efficiency by direct photoexcited

electron transfer from pollutants adsorbed on the surface valence band of BiOBr modified with graphitized C, J. Hazard. Mater., 424 (2022) 127502, doi: 10.1016/j.jhazmat.2021.127502.
[38] R. Bibi, Q. Shen, L. Wei, D. Hao, N. Li, J. Zhou, Hybrid BiOBr/UiO-66-NH_2 composite with enhanced visible-light driven photocatalytic activity toward RhB dye degradation, RSC Adv., 8 (2018) 2048–2058.
[39] A. Kumar, M. Khan, X. Zeng, I.M.C. Lo, Development of g-C_3N_4/TiO_2/Fe_3O_4@SiO_2 heterojunction via sol-gel route: a magnetically recyclable direct contact Z-scheme nanophotocatalyst for enhanced photocatalytic removal of ibuprofen from real sewage effluent under visible light, Chem. Eng. J. (Lausanne), 353 (2018) 645–656.
[40] K.S.W. Sing, D.H. Everett, R.A.W. Haul, L. Moscou, R.A. Pierotti, J. Rouquerol, T. Siemieniewska, Reporting physisorption data for gas solid systems with special reference to the determination surface-area and porosity, Pure Appl. Chem., 57 (1985) 603–619.
[41] J.S. Valente, F. Tzompantzi, J. Prince, J.G.H. Cortez, R. Gomez, Adsorption and photocatalytic degradation of phenol and 2,4-dichlorophenoxiacetic acid by Mg–Zn–Al layered double hydroxides, Appl. Catal., B, 90 (2009) 330–338.
[42] J. Di, J. Xia, Y. Ge, H. Li, H. Ji, H. Xu, Q. Zhang, H. Li, M. Li, Novel visible-light-driven CQDs/Bi_2WO_6 hybrid materials with enhanced photocatalytic activity toward organic pollutants degradation and mechanism insight, Appl. Catal., B, 168–169 (2015) 51–61.
[43] Y. Gu, Z. Xu, L. Guo, Y. Wan, ZnO nanoplate-induced phase transformation synthesis of the composite ZnS/$In(OH)_3$/In_2S_3 with enhanced visible-light photodegradation activity of pollutants, CrystEngComm, 16 (2014) 10997–11006.
[44] Y. Zhang, Z.-R. Tang, X. Fu, Y.-J. Xu, TiO_2–graphene nanocomposites for gas-phase photocatalytic degradation of volatile aromatic pollutant: is TiO_2–graphene truly different from other TiO_2–carbon composite materials?, ACS Nano, 4 (2010) 7303–7314.
[45] H. Fan, T. Jiang, H. Li, D. Wang, L. Wang, J. Zhai, D. He, P. Wang, T. Xie, Effect of $BiVO_4$ crystalline phases on the photoinduced carriers behavior and photocatalytic activity, J. Phys. Chem. C, 116 (2012) 2425–2430.
[46] K. Nagaveni, M.S. Hegde, G. Madras, Structure and photocatalytic activity of $Ti_{1-x}M_xO_{2\pm\delta}$ (M = W, V, Ce, Zr, Fe, and Cu) synthesized by solution combustion method, J. Phys. Chem. B, 108 (2004) 20204–20212.
[47] C. Du, S. Nie, C. Zhang, T. Wang, S. Wang, J. Zhang, C. Yu, Z. Lu, S. Dong, J. Feng, H. Liu, J. Sun, Dual-functional Z-scheme CdSe/Se/BiOBr photocatalyst: generation of hydrogen peroxide and efficient degradation of ciprofloxacin, J. Colloid Interface Sci., 606 (2022) 1715–1728.